



**AFRL-RQ-WP-TP-2013-0243**

**TRAVELING CROSSFLOW INSTABILITY FOR HIFIRE-5  
IN A QUIET HYPERSONIC WIND TUNNEL (POSTPRINT)**

**Matthew P. Borg**

**Booz Allen Hamilton**

**Roger L. Kimmel**

**Hypersonic Sciences Branch  
High Speed Systems Division**

**Scott Stanfield**

**Spectral Energies, LLC**

**JUNE 2013**

**Approved for public release; distribution unlimited.**

*See additional restrictions described on inside pages*

**STINFO COPY**

**AIR FORCE RESEARCH LABORATORY  
AEROSPACE SYSTEMS DIRECTORATE  
WRIGHT-PATTERSON AIR FORCE BASE, OH 45433-7542  
AIR FORCE MATERIEL COMMAND  
UNITED STATES AIR FORCE**

## NOTICE AND SIGNATURE PAGE

Using Government drawings, specifications, or other data included in this document for any purpose other than Government procurement does not in any way obligate the U.S. Government. The fact that the Government formulated or supplied the drawings, specifications, or other data does not license the holder or any other person or corporation; or convey any rights or permission to manufacture, use, or sell any patented invention that may relate to them.

This report was cleared for public release by the USAF 88th Air Base Wing (88 ABW) Public Affairs Office (PAO) and is available to the general public, including foreign nationals.

Copies may be obtained from the Defense Technical Information Center (DTIC)  
(<http://www.dtic.mil>).

AFRL-RQ-WP-TP-2013-0243 HAS BEEN REVIEWED AND IS APPROVED FOR  
PUBLICATION IN ACCORDANCE WITH ASSIGNED DISTRIBUTION STATEMENT.

\*//Signature//

---

ROGER L. KIMMEL  
Project Manager  
Hypersonic Sciences Branch  
High Speed Systems Division

//Signature//

---

MARK AMENDT, Chief  
Hypersonic Sciences Branch  
High Speed Systems Division  
Aerospace Systems Directorate

This report is published in the interest of scientific and technical information exchange, and its publication does not constitute the Government's approval or disapproval of its ideas or findings.

\*Disseminated copies will show “//Signature//” stamped or typed above the signature blocks.

REPORT DOCUMENTATION PAGE				Form Approved OMB No. 0704-0188	
<p>The public reporting burden for this collection of information is estimated to average 1 hour per response, including the time for reviewing instructions, searching existing data sources, gathering and maintaining the data needed, and completing and reviewing the collection of information. Send comments regarding this burden estimate or any other aspect of this collection of information, including suggestions for reducing this burden, to Department of Defense, Washington Headquarters Services, Directorate for Information Operations and Reports (0704-0188), 1215 Jefferson Davis Highway, Suite 1204, Arlington, VA 22202-4302. Respondents should be aware that notwithstanding any other provision of law, no person shall be subject to any penalty for failing to comply with a collection of information if it does not display a currently valid OMB control number. <b>PLEASE DO NOT RETURN YOUR FORM TO THE ABOVE ADDRESS.</b></p>					
1. REPORT DATE (DD-MM-YY) June 2013		2. REPORT TYPE Conference Paper Postprint		3. DATES COVERED (From - To) 30 June 2012 – 30 June 2013	
4. TITLE AND SUBTITLE TRAVELING CROSSFLOW INSTABILITY FOR HIFIRE-5 IN A QUIET HYPERSONIC WIND TUNNEL (POSTPRINT)				5a. CONTRACT NUMBER In-house	
				5b. GRANT NUMBER	
				5c. PROGRAM ELEMENT NUMBER 61102F	
6. AUTHOR(S) Matthew P. Borg (Booz Allen Hamilton) Roger L. Kimmel (AFRL/RQHF) Scott Stanfield (Spectral Energies, LLC)				5d. PROJECT NUMBER 2307	
				5e. TASK NUMBER	
				5f. WORK UNIT NUMBER Q042	
7. PERFORMING ORGANIZATION NAME(S) AND ADDRESS(ES) Hypersonic Sciences Branch (AFRL/RQHF) High Speed Systems Division, Air Force Research Laboratory Aerospace Systems Directorate Wright-Patterson Air Force Base, OH 45433-7542 Air Force Materiel Command, United States Air Force			Booz Allen Hamilton ----- Spectral Energies, LLC		8. PERFORMING ORGANIZATION REPORT NUMBER  AFRL-RQ-WP-TP-2013-0243
9. SPONSORING/MONITORING AGENCY NAME(S) AND ADDRESS(ES) Air Force Research Laboratory Aerospace Systems Directorate Wright-Patterson Air Force Base, OH 45433-7542 Air Force Materiel Command United States Air Force				10. SPONSORING/MONITORING AGENCY ACRONYM(S) AFRL/RQHF	
				11. SPONSORING/MONITORING AGENCY REPORT NUMBER(S) AFRL-RQ-WP-TP-2013-0243	
12. DISTRIBUTION/AVAILABILITY STATEMENT Approved for public release; distribution unlimited.					
13. SUPPLEMENTARY NOTES PA Case Number: 88ABW-2013-2537; Clearance Date: 04 Jun 2013. This paper contains color. The conference paper was presented at the 43rd Fluid Dynamics Conference, held in San Diego, California, from June 24 through 27, 2013, and was published in the AIAA Proceedings of the 43rd Fluid Dynamics Conference.  The U.S. Government is joint author of the work and has the right to use, modify, reproduce, release, perform, display, or disclose the work.					
14. ABSTRACT A scale model of the 2:1 elliptic cone HIFIRE-5 flight vehicle was used to investigate the traveling crossflow instability at Mach 6 in Purdue University's Mach-6 quiet wind tunnel. Traveling crossflow waves were measured with surface-mounted pressure sensors. The crossflow instability phase speed and wave angle were calculated from the cross spectra of three surface-mounted pressure sensors. Both quantities show good agreement with computational values from about 30 to 50 kHz. Repeated runs at the same initial condition show excellent repeatability in traveling crossflow wave properties, and give an estimate of the Experimental uncertainty associated with this technique. Additionally, autobispectral analysis showed the onset and development of moderate nonlinear quadratic phase-locking prior to transition, but not for the peak traveling crossflow wave. The bicoherence achieved only moderate values. No traveling crossflow waves were observed when freestream noise levels were intentionally elevated, but transition occurred for a much lower Reynolds number. It appears that the traveling crossflow instability is not the primary transition mechanism in the noisy flow of Purdue's Mach 6 wind tunnel.					
15. SUBJECT TERMS Boundary layer transition, hypersonic, flight test					
16. SECURITY CLASSIFICATION OF:			17. LIMITATION OF ABSTRACT: SAR	18. NUMBER OF PAGES 24	19a. NAME OF RESPONSIBLE PERSON (Monitor) Roger L. Kimmel 19b. TELEPHONE NUMBER (Include Area Code) N/A
a. REPORT Unclassified	b. ABSTRACT Unclassified	c. THIS PAGE Unclassified			

# Traveling Crossflow Instability for HIFiRE-5 in a Quiet Hypersonic Wind Tunnel

Matthew P. Borg,<sup>\*</sup> Roger L. Kimmel,<sup>†</sup> and Scott Stanfield<sup>‡</sup>

*Air Force Research Laboratory, Air Vehicles Directorate  
2130 8th St., WPAFB, OH 45433-7542, USA*

## Abstract

A scale model of the 2:1 elliptic cone HIFiRE-5 flight vehicle was used to investigate the traveling crossflow instability at Mach 6 in Purdue University's Mach-6 quiet wind tunnel. Traveling crossflow waves were measured with surface-mounted pressure sensors. The crossflow instability phase speed and wave angle were calculated from the cross spectra of three surface-mounted pressure sensors. Both quantities show good agreement with computational values from about 30-50 kHz. Repeated runs at the same initial condition show excellent repeatability in traveling crossflow wave properties, and give an estimate of the experimental uncertainty associated with this technique. Additionally, autobispectral analysis showed the onset and development of moderate nonlinear quadratic phase-locking prior to transition, but not for the peak traveling crossflow wave. The bicoherence achieved only moderate values. No traveling crossflow waves were observed when freestream noise levels were intentionally elevated, but transition occurred for a much lower Reynolds number. It appears that the traveling crossflow instability is not the primary transition mechanism in the noisy flow of Purdue's Mach 6 wind tunnel.

## I. Introduction

The Hypersonic International Flight Research Experimentation (HIFiRE) program is a hypersonic flight test program jointly executed by the Air Force Research Laboratory (AFRL) and the Australian Defence Science and Technology Organization (DSTO).<sup>1,2</sup> The purpose of this research is to develop and validate technologies critical to the development of next generation hypersonic aerospace systems. Candidate technology areas include, but are not limited to, propulsion, propulsion-airframe integration, aerodynamics and aerothermodynamics, high temperature materials and structures, thermal management strategies, guidance, navigation, and control, sensors, and system components. The HIFiRE program consists of extensive ground tests and computation focused on specific hypersonic flight technologies. Each technology program culminates in a flight test. HIFiRE-5 is the second of two flights in the HIFiRE manifest focused on boundary layer transition. The HIFiRE-1 program created an extensive knowledge base regarding transition on axisymmetric bodies that has been summarized in numerous prior publications.<sup>3-14</sup> The HIFiRE-5 flight is devoted to measuring transition on a three-dimensional (3D) body.

Extended hypersonic flight with lifting configurations requires improved understanding and prediction of 3D transition. Transition on 3D configurations embodies several phenomena not encountered on axisymmetric configurations like HIFiRE-1, including leading-edge or attachment-line transition and crossflow instabilities (including crossflow interactions with other instability mechanisms shared with axisymmetric flow configurations such as first and second mode instabilities). Very limited hypersonic flight data exist for any of these phenomena.<sup>15</sup> The need for a better understanding of 3D transition motivates the HIFiRE-5 experiment.

<sup>\*</sup>Booz Allen Hamilton, 937-713-6697, matthew.borg@wpafb.af.mil

<sup>†</sup>AFRL, 937-255-8295, roger.kimmel@wpafb.af.mil

<sup>‡</sup>Spectral Energies, LLC., 937-713-6713, scott.stanfield.ctr@wpafb.af.mil

This material has been cleared for public release. Case Number 88ABW-2013-2537.

Approved for public release; distribution unlimited.

1 of 17

American Institute of Aeronautics and Astronautics

Accurately simulating flight conditions in a pre-flight, ground-test environment is very challenging. One often overlooked issue is that of tunnel noise. Conventional supersonic and hypersonic wind tunnels are characterized by high levels of freestream noise. This noise takes the form of eddy Mach wave acoustic energy radiated from the turbulent wall boundary layer. Root-mean-square pitot pressure fluctuations are typically on the order of 0.5-1.0% of the mean for conventional hypersonic tunnels. Reference 16 summarizes noise measurements from many supersonic and hypersonic wind tunnels for Mach numbers ranging from 2 to 24. Flight noise levels, however, can be an order of magnitude lower than those experienced in conventional hypersonic ground facilities.<sup>17, 18</sup>

Elevated noise levels have been shown to decrease the transition Reynolds number by up to an order of magnitude and even change or bypass the normal parametric trends in transition.<sup>19, 20</sup> Reference 17 presents an extensive review of the effect of tunnel noise on transition. References 8, 21 and 22 report an effect of freestream noise on roughness-induced transition. The high levels of noise in conventional tunnels introduce uncertainty in using transition data from conventional facilities to predict transition on flight vehicles.<sup>23</sup>

## I.A. Vehicle Description

The HIFiRE-5 configuration consists of a payload mounted atop an S-30 first stage<sup>24</sup> and Improved Orion<sup>25</sup> second stage motor, shown in Figure 1. The term payload refers to all test equipment mounted to the second stage booster, including the instrumented test article and additional control and support sections situated between the test article and the second stage motor. The test article consists of a blunt-nosed elliptic cone of 2:1 ellipticity, 0.86 meters in length.

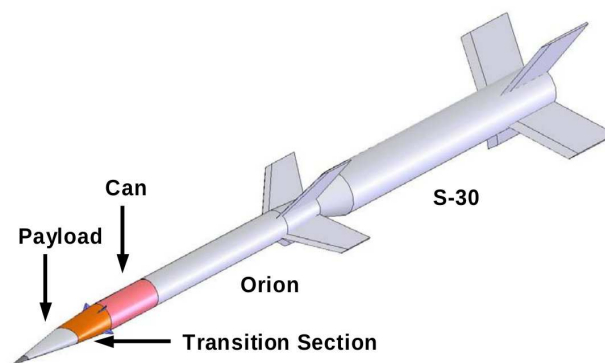


Figure 1: HIFiRE-5 stack

The elliptic cone configuration was chosen as the test-article geometry based on extensive previous testing and analysis on elliptic cones.<sup>26-33</sup> This prior work<sup>26-28</sup> demonstrated that the 2:1 elliptic cone would generate significant crossflow instability at the expected flight conditions. The 2:1 elliptic cone configuration also possesses ample internal volume for sensors and instrumentation. In order to exploit this prior body of work and expedite configuration development, the 2:1 elliptical geometry was selected as the HIFiRE-5 test article. The half-angle of the elliptic cone test article in the minor axis ( $x$ - $y$ ) plane is  $7.00^\circ$ , and  $13.80^\circ$  in the major axis, where  $x$  is the streamwise direction and  $y$  is the spanwise direction. The nose tip cross-section in the minor axis is a 2.5 mm radius circular arc, tangent to the cone ray describing the minor axis, and retains a 2:1 elliptical cross-section to the stagnation point.

## II. Traveling Crossflow Instability

For 3D vehicle configurations with significant crossflow, the crossflow instability can become the dominant path to boundary layer transition. Both stationary and traveling modes are possible with stationary vortices nearly aligned with the inviscid streamline direction, and traveling waves inclined at a steep angle to the inviscid streamlines. The wave vector of the most unstable traveling mode has a spanwise component opposite to the direction of the crossflow.<sup>34</sup> For incompressible flows the stationary modes are typically dominant in low noise environments of flight and “quiet” wind tunnels, while the traveling modes tend to dominate in conventional tunnels.<sup>35</sup> The stationary mode is thought to be seeded by natural surface roughness, while the traveling mode is generated by vortical disturbances in the freestream which are entrained in the boundary

layer.<sup>36</sup> Saric<sup>35,37</sup> suggested that the same behavior should be seen for compressible flows.

Considerable effort has been given to crossflow instabilities for incompressible flow.<sup>36,38–40</sup> Saric and Reed<sup>35</sup> detail the pertinence of nonlinear effects when predicting crossflow instability growth and transition for incompressible flow. It has been well established that stationary modes, after a period of linear growth, saturate nonlinearly and give rise to secondary instabilities that then rapidly lead to transition (see, for instance, Reference 41). Most of the extant crossflow work has focused on stationary modes, since this is expected to be the dominant crossflow instability in the low-noise flight environment.

Despite much effort to understand the crossflow instability, little of it has focused on the hypersonic regime. King<sup>42</sup> made measurements of crossflow-dominated transition at Mach 3.5 in quiet and noisy flow. Poggie and Kimmel<sup>43</sup> measured traveling crossflow waves at Mach 8 on an elliptic cone with hot films, but were not able to get good agreement with computational results. They suggest that the poor agreement was due to the limitations of the computations. Malik<sup>15</sup> detailed results from a crossflow-dominated hypersonic flight test including stability computations. Choudhari<sup>44</sup> details stability computations for HIFiRE-5 for both flight and wind tunnel conditions. Swanson<sup>45</sup> measured stationary crossflow vortices at Mach 6 in a quiet wind tunnel. Reference 46 describes previous experiments for the HIFiRE-5 geometry that primarily focused on stationary crossflow modes in the BAM6QT. Traveling crossflow waves were also detected, but were not the main focus of the previous studies.

Although the highly nonlinear development of the crossflow instability modes has been well-documented for incompressible flows, the contribution of nonlinear processes at hypersonic Mach numbers is not well understood. The current experiments attempt to verify the presence of the traveling crossflow instability as well as help establish the extent of nonlinear interactions for the traveling crossflow instability in the hypersonic regime. Experimental crossflow instability properties are compared to computations to verify that the measured disturbances are crossflow and not some other instability mechanism.

## II.A. Model Description

The model, shown in Figure 2, is a 38.1% scale model of the flight vehicle. It includes the vehicle features from the nose to the payload/transition-section interface. The model is 328.1 mm long and has a base diameter of 164.6 mm in the major-axis direction and maintains 2:1 ellipticity from the base to the tip. The 76.2 mm long nosetip is fabricated from 15-5 stainless steel, followed by a frustum made of 7075T6 aluminum. For the present experiments, much of the model acreage was spray-painted black. The paint was left on the model after previous florescent oil flow visualization. The edges of the paint were sanded with fine-grit sand paper to more smoothly transition the model surface from the bare aluminum finish to the paint layer. A more complete description of the model can be found in Reference 47.



Figure 2: Wind tunnel model

## III. Experimental Overview

Experiments were performed in Purdue University's Boeing AFOSR /Mach-6 Quiet Tunnel (BAM6QT). Quiet flow was realized for freestream Reynolds numbers up to  $12.2 \times 10^6/\text{m}$ . The Purdue tunnel achieves

Approved for public release; distribution unlimited.

3 of 17

American Institute of Aeronautics and Astronautics

quiet noise levels by maintaining a laminar boundary layer on the tunnel walls. A laminar boundary layer is achieved by removing the nozzle boundary layer just upstream of the throat via a bleed suction system. A new, laminar boundary layer then begins near the nozzle throat. The boundary layer is kept laminar by maintaining a highly-polished nozzle wall to reduce roughness effects. The divergence of the nozzle is intentionally very gradual to mitigate the centrifugal Görtler instability on the tunnel walls.<sup>48</sup> The experimental results presented in this paper were obtained with the model at 0 degrees angle of attack and yaw.

Kulite XCQ-062-15A and XCE-062-15A pressure transducers with A screens were mounted flush with the model surface to detect traveling crossflow waves. The Kulite sensors are mechanically stopped at about 1 bar so that they can survive the full stagnation pressure in the BAM6QT and still maintain the sensitivity of a 1 bar full-scale sensor. These sensors typically have flat frequency response up to about 30-40% of their roughly 270-285 kHz resonant frequency.<sup>49</sup>

For the current experiments, five instrumentation holes were available in the model. Table 1 shows the locations of the instrumentation holes. Figure 3 shows a sketch of the model and sensor holes. The holes were located in a region of the model that had previously shown strong stationary crossflow vortices.<sup>46,47,50</sup> Although there were five holes, there were only four available pressure sensors for most of the quiet experiments, so some repositioning of the sensors was necessary to gather data from all five sensor hole locations.

Hole Number	$x$ (mm)	$y$ (mm)
1	310.14	41.21
2	312.56	45.09
3	312.56	39.78
4	315.48	43.04
5	318.07	39.78

Table 1: Instrumentation hole locations and notation

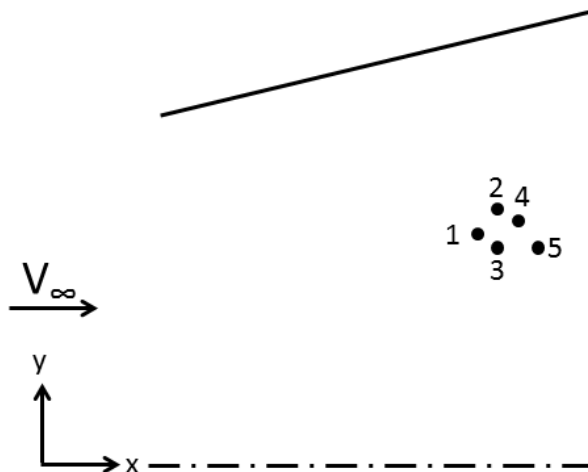


Figure 3: Schematic of instrumentation holes

## IV. Reynolds Number Sweep

### IV.A. Spectra

Sixteen unique runs comprised a Reynolds number sweep from  $Re=5.9-12.2 \times 10^6/m$  with a fine gradation in Reynolds number (changes of about 35 kPa in initial stagnation pressure). This allowed the development and evolution of the traveling crossflow waves to be studied in great detail. Figure 4 shows power spectral densities (PSD) for some of the Reynolds numbers tested for sensors 1, 3, and 5. A sensor was also installed in hole 4, but at some unknown point during the experiments, it came loose from the hole. Thus, data from

sensor 4 are regarded as unreliable and are not shown.

Data were sampled at 5 MHz. The time traces at the conditions of interest were divided into 243 windowed segments of 4096 samples, meaning that each PSD is for 199 ms of data. For the BAM6QT, the time it takes for the expansion wave to traverse the length of the driver tube, reflect, and return is approximately 200 ms. Thus, each PSD is computed for quasi-steady conditions with at most one 5-6% reduction in Reynolds number due to the reflecting expansion wave. Freestream Reynolds numbers were estimated using the method developed in Reference 51. Uncertainty in the calculated freestream Reynolds number is largely due to 2 s of massively separated nozzle wall boundary layer just subsequent to tunnel startup.

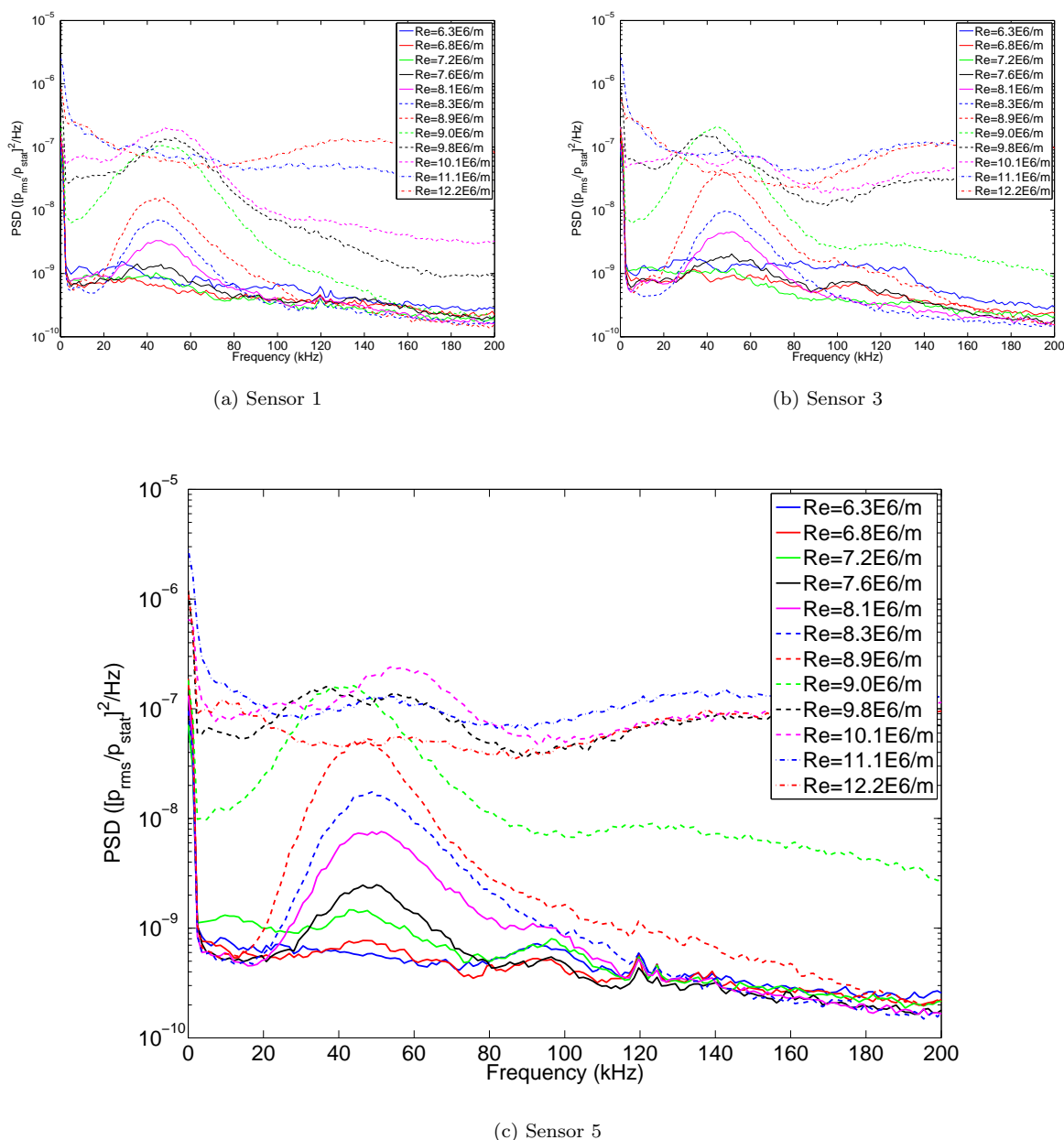


Figure 4: PSDs for quiet Reynolds number sweep, sensors 1, 3, and 5

For all three sensor locations, the spectra at  $Re=6.3 \times 10^6/m$  appear to be laminar without measurable disturbances. For each sensor, as  $Re$  is increased, a small peak in the spectra centered near 45 kHz begins to grow above the laminar spectra, which is essentially the noise floor. The magnitude of the peak centered at



45 kHz continues to increase with  $Re$  until apparent transition onset is evidenced by peak broadening and elevated power at all frequencies. As  $Re$  continues to increase, the main 45 kHz disturbance peak begins to be overwhelmed by power at all other frequencies as the boundary layer begins to transition. For the highest Reynolds numbers, the boundary layer is fully turbulent, and little or no evidence of the traveling crossflow waves remains.

For sensors 1 and 3, the 45 kHz traveling wave is not seen until  $Re=7.2-7.6 \times 10^6/m$ . For sensor 5, the disturbance can barely be seen for  $Re=6.8 \times 10^6/m$ . For sensor 1, the boundary layer has not completely transitioned at the highest Reynolds number. The spectra for  $Re=11.1$  and  $12.2 \times 10^6/m$  do not quite fall on top of each other. For sensors 3 and 5, however, the spectra for  $Re=11.1$  and  $12.2 \times 10^6/m$  fall nearly on top of each other, indicating that the boundary layer at sensors 3 and 5 is turbulent for  $Re \geq 11.1 \times 10^6/m$ . Additionally, the unit Reynolds numbers for which spectral broadening starts to be significant decreases with increasing downstream sensor location.

Computations for  $Re=8.3 \times 10^6/m$  predicted a peak N factor of 11.5 for traveling crossflow waves near the sensor locations at 40 kHz,<sup>52</sup> in good agreement with the experimental peak shown in Figure 4. For reference, an N-factor contour plot, reproduced from Reference 44, for traveling crossflow at  $Re=9.8 \times 10^6/m$  is shown in Figure 5. The computations for  $Re=8.1 \times 10^6/m$  also show that the pressure eigenfunction for traveling crossflow waves near the sensor locations has its peak amplitude away from the surface. However, the amplitude at the surface is still around 73% of the peak amplitude.<sup>52</sup> Thus, conditions are not unfavorable for detection of traveling crossflow waves with surface-mounted pressure sensors. All of these data are consistent with traveling 45 kHz crossflow instability waves that grow in amplitude for increasing Reynolds number.

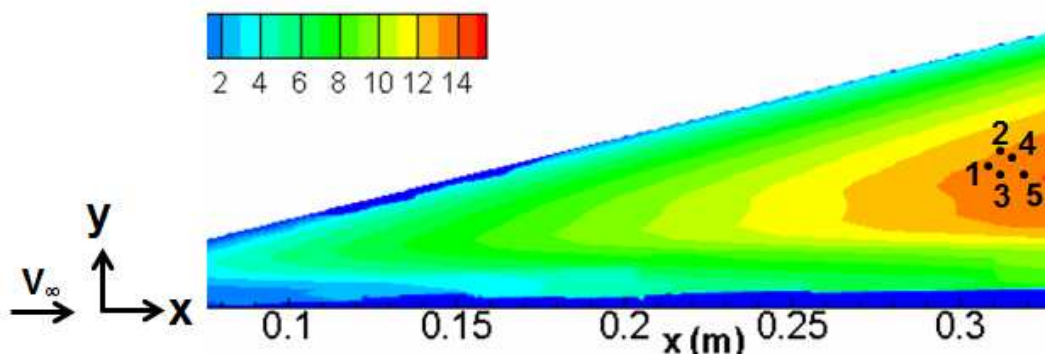


Figure 5: N-factor contour for traveling crossflow for  $Re=9.8 \times 10^6/m$ . Reproduced from Reference 44. Sensor locations and notation added.

#### IV.B. Calculation of Crossflow Wave Properties

The utilization of four sensors allows the calculation of disturbance phase speed and wave angle as a function of frequency using the cross spectrum. Although the more general case allows four sensors, the minimum number of sensors needed to calculate the quantities of interest is three, since two unique sensor pairs are needed. The method of Reference 53 as used in Reference 43 was followed to calculate the wave angle and phase speed. The autospectrum of a sensor's signal is given by

$$G(f) = 2 \lim_{T \rightarrow \infty} (1/T) E[|\hat{s}(f, T)|^2] \quad (1)$$

Here, the Fourier transform of a measured signal  $s(t)$  is  $\hat{s}(f)$ , and the expected value operator is  $E[\cdot]$ .

The cross spectrum of two signals is similarly

$$S_{12}(f) = \lim_{T \rightarrow \infty} (1/T) E[\hat{s}_1^*(f, T) \hat{s}_2(f, T)] \quad (2)$$

where  $*$  denotes a complex conjugate. A convenient, real-valued method of measuring the amplitude of the cross spectrum is the coherence, given by

$$\gamma^2(f) = \frac{|S_{12}(f)|^2}{S_{11}(f)S_{22}(f)} \quad (3)$$

The coherence is essentially a frequency-dependent cross correlation of the signals. The normalization factor is the maximum value that the cross spectrum can achieve. Thus, normalizing by this value yields coherence values from 0 to 1, with 0 meaning no correlation between the signals and 1 signifying perfect correlation.

The phase spectrum can then be found by

$$\Theta(f) = \arctan \left( \frac{\Im[S_{12}]}{\Re[S_{12}]} \right) \quad (4)$$

where  $\Im[\cdot]$  and  $\Re[\cdot]$  represent the real and imaginary components, respectively.

The time delay associated with the phase spectrum is given by

$$\tau(f) = \Theta(f)/2\pi f \quad (5)$$

An arbitrary configuration of four probes and incident planar waves is sketched in Figure 6a. Rotating the coordinate system by  $\Psi$ , the angle between the wave propagation direction and the  $\epsilon$  axis, transforms the arrangement to that shown in Figure 6b. Here,  $\epsilon$  and  $\eta$  are the axial and circumferential surface coordinates projected onto the  $x - y$  plane. This method is valid for regions of small local surface curvature.

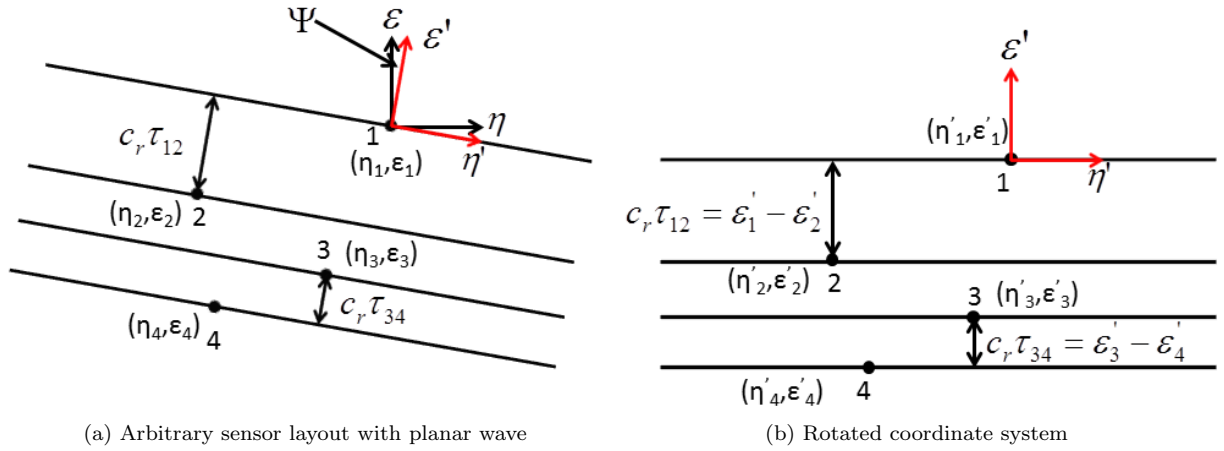


Figure 6: Notional sensor layout for cross-spectral analysis

The relation between points in the original coordinate system  $(\epsilon, \eta)$  and the rotated system  $(\epsilon', \eta')$  is given by

$$\eta' = \eta \cos \Psi - \epsilon \sin \Psi \quad (6)$$

$$\epsilon' = \eta \sin \Psi + \epsilon \cos \Psi \quad (7)$$

The time delay between the arrival of a particular phase surface at sensors  $a$  and  $b$  is given by

$$c_r \tau_{12} = \epsilon'_1 - \epsilon'_2 \quad (8)$$

where  $c_r$  is the phase speed and  $\tau_{12}$  is the time delay between a particular phase surface arriving at sensors 1 and 2. Two unique sensor pair sets  $ab$  and  $cd$  are chosen. Here,  $a, b, c$ , and  $d$  can be any of the four sensors, subject to the constraints that  $a \neq b$  and  $c \neq d$ . Using Equations 7 and 8 for both sensor pairs and solving the resultant system of equations, the propagation angle,  $\Psi$  and phase speed,  $c_r$  can be found from

$$\Psi = \arctan \left[ \frac{\tau_{ab}(\epsilon_d - \epsilon_c) - \tau_{cd}(\epsilon_b - \epsilon_a)}{-\tau_{ab}(\eta_d - \eta_c) + \tau_{cd}(\eta_b - \eta_a)} \right] \quad (9)$$

and

$$c_r = \frac{\sin \Psi(\eta_a - \eta_b) + \cos \Psi(\epsilon_a - \epsilon_b)}{\tau_{ab}} \quad (10)$$

#### IV.C. Traveling Crossflow Wave Properties

Using Equations 9 and 10 and the pressure traces from sensors 1, 3, and 5, the wave angle and phase velocity of the traveling crossflow waves were calculated for  $Re=6.8-9.0 \times 10^6/m$ . Typical plots of PSD, coherence, phase delay, and time delay for  $Re=8.5 \times 10^6/m$  are shown in Figure 7.

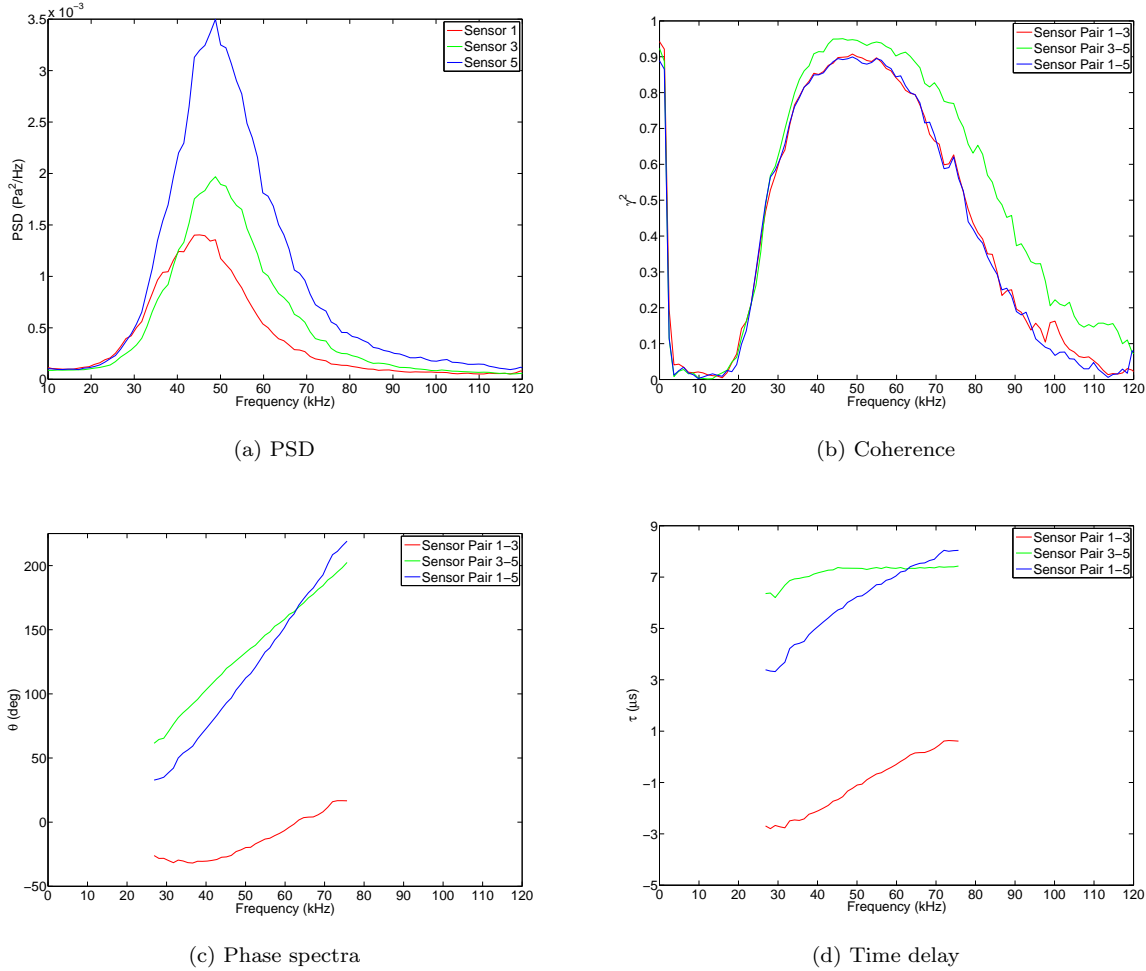


Figure 7: Typical PSD,  $\gamma^2$ ,  $\Theta$ , and  $\tau$  for  $Re=8.5 \times 10^6/m$

Figure 8 shows  $\Psi$  and  $c_r$  for  $Re=6.8-9.0 \times 10^6/m$ . Additionally, a few computational data points for traveling crossflow are shown.<sup>54</sup> For portions of the spectra with low coherence ( $\lesssim 0.2$ ), there are little or no correlated disturbances common among the sensors, and derived quantities such as  $\Psi$  and  $c_r$  are meaningless. The coherence was typically greatest for  $25 \leq f \leq 80$  kHz and insignificant outside this band. Thus,  $\Psi$  and  $c_r$  are shown only for this frequency band.

Here,  $\Psi$  is the direction of propagation of wavefronts with respect to the  $x$  axis. Thus, for a wave angle of  $\Psi=70^\circ$ , lines tangent to the wavefronts are inclined  $20^\circ$  with respect to the  $x$  axis, and propagate in an outward direction inclined  $20^\circ$  downstream of the  $y$  axis. As shown in Figure 8a, good agreement among the various Reynolds numbers and with the computational curve is seen for  $6.8 \leq Re \leq 8.5 \times 10^6/m$ . For the two highest Reynolds numbers shown,  $Re=8.9$  and  $9.0 \times 10^6/m$ , the curves diverge significantly from those in good agreement with each other. This attributed to nonlinear processes becoming significant at these higher Reynolds numbers. Evaluation of the cross spectrum assumes linear processes. When nonlinear

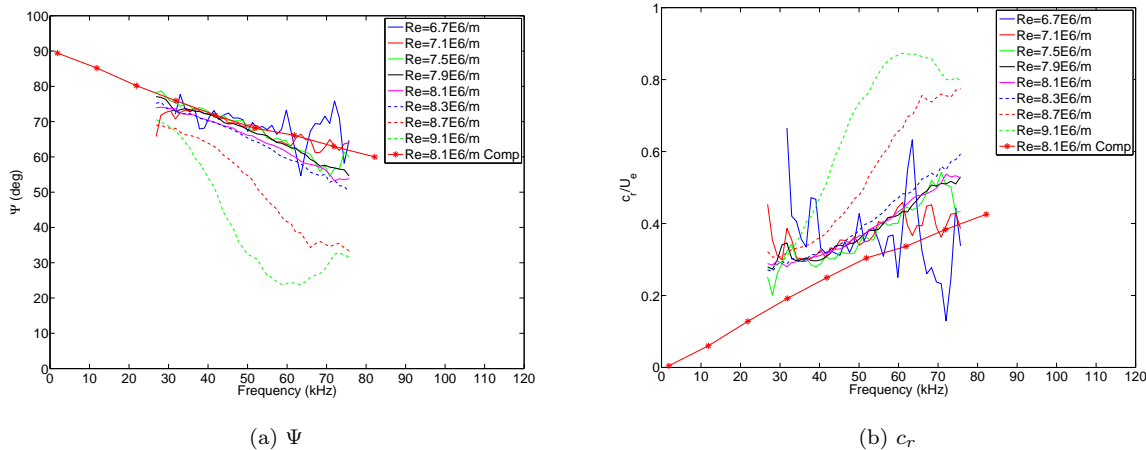


Figure 8:  $\Psi$  and  $c_r$  for traveling crossflow instability

effects become significant, this assumption is no longer valid and the resultant quantities lose significance. The observed nonlinearities are further investigated and discussed in Section VI.

In the range of 30-55 kHz, the experimentally calculated values of  $\Psi$  for  $Re=6.8-8.5 \times 10^6/m$  match both the values and slope of the computations. Above 55 kHz, the computational values of  $\Psi$  depart from the nearly linear trend with frequency exhibited for lower frequencies. Here, the computational values depart from the experimental wave angles by as much as 15%. In the range of 30-55 kHz, the computationally calculated values of  $c_r$  vary from 35% at 30 kHz and decrease to about 15% below the experimental values at 55 kHz. For frequencies above 55 kHz, the difference increases to about 25%.

For both  $\Psi$  and  $c_r$ , the curves for  $Re=6.8-8.5 \times 10^6/m$  show good agreement among themselves, even though they differ from the computational values. It is somewhat surprising that the wave angles over a range of Reynolds numbers and disturbance frequency agree so well with the computational values, while the experimental  $c_r$  is markedly higher than the computation for all frequencies and Reynolds numbers.

The reason for this discrepancy is unknown, but is possibly due to experimental uncertainties such as sensor hole locations and the fact that sensors do not provide point measurements, but rather an integrated value over a finite area. For both  $\Psi$  and  $c_r$ , the curves for  $Re=6.8 \times 10^6/m$  show a considerable amount of scatter. This is because the surface pressure signature of the traveling crossflow waves is very small at this low Reynolds number, resulting in low coherence and more scatter in the measured values of  $\Psi$  and  $c_r$ .

Neither  $\Psi$  nor  $c_r$  seem to exhibit any major dependence on Reynolds number for  $Re=6.8-8.5 \times 10^6/m$ . It does appear that  $\Psi$  becomes slightly more sensitive to frequency as  $Re$  increases. The lack of any significant dependence on Reynolds number is possibly due to the fairly narrow Reynolds number range for which nonlinear processes are absent and for which the crossflow waves are of measureable amplitude,  $Re=6.8-8.5 \times 10^6/m$ . This is a fairly modest increase in  $Re$  of only 24%. If the boundary layer thickness scales with  $1/\sqrt{Re}$ , this is a decrease in boundary layer thickness of only 10%. If  $\Psi$  and  $c_r$  scale with the boundary layer thickness, changes in these quantities could be overwhelmed by the uncertainties of the measurements.

## V. Repeatability at $Re=8.1E6/m$

Repeatability was checked with duplicate runs for all Reynolds numbers. For  $Re=8.1 \times 10^6/m$ , 11 separate runs were performed. The results are shown in Figure 9.

Figure 9a shows PSDs for 11 runs at  $Re=8.1 \times 10^6/m$ . Excellent agreement is shown for the peak frequency of about 45-47 kHz. However, the root-mean-square (RMS) amplitude of the disturbance varies by about a factor of 2.8. Runs 25, 29, 32, 33, and 36 were completed over several days with various other runs at different conditions in between them. Runs 37-42 were completed consecutively on the same day with a 40-60 minute delay between runs. There is no obvious trend for the RMS amplitudes of the PSDs for runs 25, 29, 32, 33, and 36. Runs 37-42 exhibit a clear trend, however. Each subsequent run shows a marked increase in peak amplitude. Over the span of those 6 runs, the amplitude increased by a factor of about 1.9.

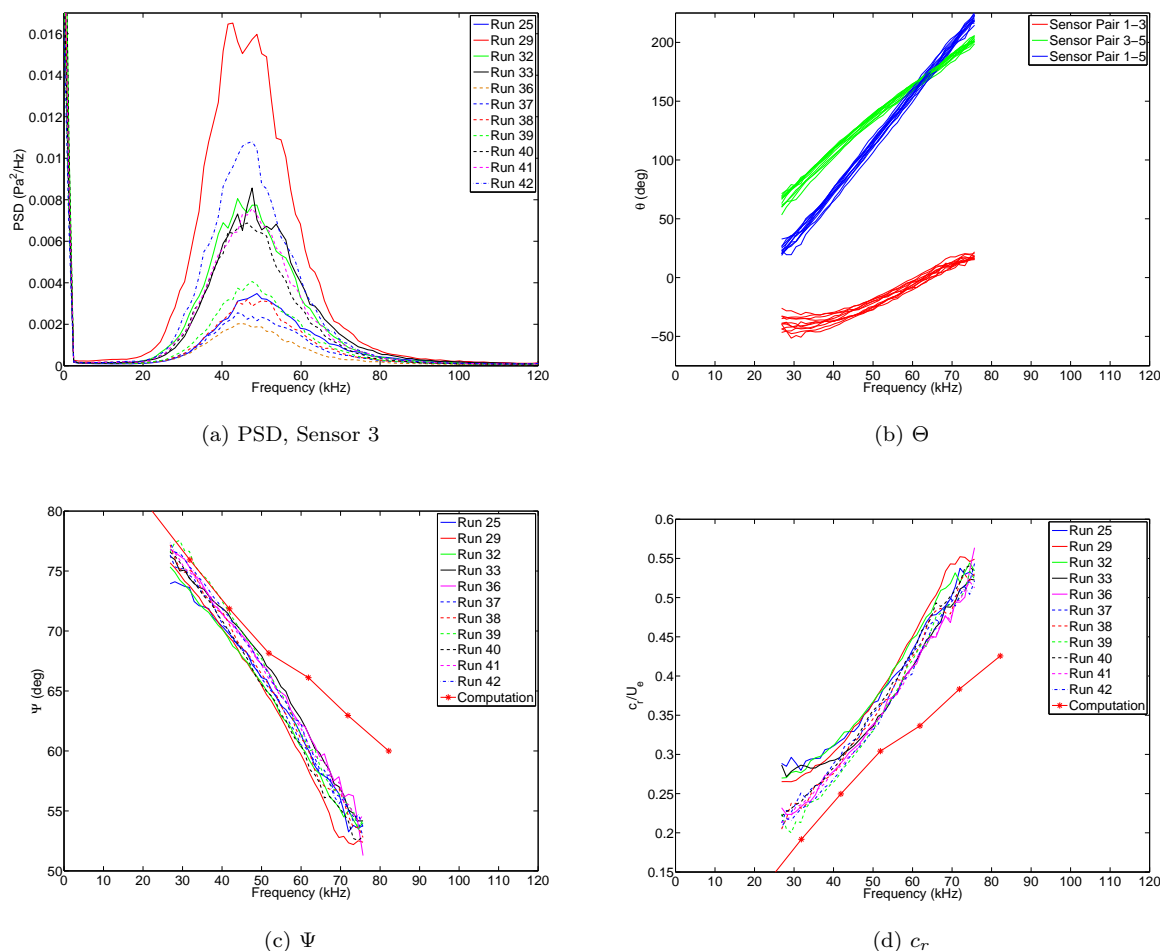


Figure 9: PSD,  $\Theta$ ,  $\Psi$ , and  $\tau$  for 11 runs with  $Re=8.1 \times 10^6/m$

The exact cause of this apparent amplitude increase is unknown.

It is possible that the change is due to the increasing temperature of the model throughout the course of a day. With each run, the model temperature increases due to convective heating while the air is flowing over the model. It is generally time prohibitive to allow the model to return to room temperature before each subsequent run. The increase in model surface temperature from the beginning of Run 37 to the end of Run 42 is estimated to be on the order of 10-15 K, as measured in Reference 55. It is possible that this temperature increase modifies the calibration of the pressure sensors, causes the model to expand altering the fit of the sensors in the holes and thus the sensor output, or that the increased surface temperature destabilizes the traveling crossflow instability, leading to larger amplitudes.

The Kulite sensors are quoted as being temperature compensated in the range from 299 to 353 K. Per Kulite specifications, in this range, the thermal zero shift is  $\pm 1\%$  full scale per 56 K temperature change. The thermal sensitivity change is  $\pm 1\%$  per 56 K temperature change. For a 15 K temperature increase, the expected thermal zero shift is about 300 Pa. The calibration slope would change by about 25 Pa/V. The resultant change in the PSD amplitudes from the change in the calibration curve due to a 15 K temperature increase is estimated to be less than 1%. It seems unlikely that shifts in the Kulite calibration due to temperature changes can account for the observed amplitude variations.

It would be somewhat surprising if such modest temperature changes, about 5%, would destabilize the traveling crossflow instability to this degree, a shift in N-factor of about  $N=\ln(2.8/1)=1.0$ . However, Malik et al.<sup>15</sup> found that a large surface temperature increase of about 100 K increased the computed stationary crossflow N-factor by about 10 at Mach 4-5. Scaling these results linearly to the present data suggests an N-factor increase of 1.5.

Approved for public release; distribution unlimited.

10 of 17

American Institute of Aeronautics and Astronautics

Although this result suggests that increased surface temperature destabilizes the crossflow instability, the surface temperatures observed by Malik et al. were an order of magnitude larger than those observed during the present experiments. Eppink<sup>56</sup> found that a small surface temperature increase of 3.9 K at Mach 0.24 increased the N-factor by 0.32. This N-factor change represents an amplitude increase of 38%. The experimentally measured amplitude change was 23%. The findings of Malik and Eppink suggest that the observed PSD amplitude increase in the present experiments may be due to destabilization of the boundary layer by the increased surface temperature. Investigation into this effect is ongoing.

Figure 9b shows values of  $\Theta_{31}$ ,  $\Theta_{35}$ , and  $\Theta_{15}$  for all 11 runs at  $Re=8.1 \times 10^6/m$ . Here, the subscripted numbers refer to the sensors of interest (e.g.  $\Theta_{31}$  refers to the phase difference between the signals for sensors 3 and 1). In this case, the band of curves are colored to correspond to the phase delay between two particular sensors. The standard deviation of each  $\Theta$  band can be used to give an estimate of experimental uncertainty. Figures 9c and 9d show values of  $\Psi$  and  $c_r$ , as well as the computational data points, for all 11 runs. As shown, both  $\Psi$  and  $c_r$  are very repeatable. Excellent agreement with the computation is shown for  $\Psi$  for frequencies between 30-55 kHz. The agreement is not as good for higher frequencies, but still within about 15% of the computations. The agreement in  $c_r$  is not quite as good, but is still close. Table 2 shows the mean, standard deviation, and range of  $\Theta$ ,  $\Psi$ , and  $c_r$  for the 11 runs. These statistics will be used to quantify uncertainty in the measurements. Despite the large range in PSD amplitude, no such variation is evident in  $\Theta$ ,  $\Psi$ , or  $c_r$ . There is also no discernible trend in these variables with increasing model temperature. Evidently, if the surface temperature is destabilizing the boundary layer, it does not impact the frequency, phase speed, or wave angle of the traveling crossflow waves.

	$\Theta_{31}$ (deg)	$\Theta_{35}$ (deg)	$\Theta_{51}$ (deg)	$\Psi$ (deg)	$c_r$ ( $u/U_e$ )
Low Value	29.8	101.4	65.0	70.2	0.26
High Value	41.8	110.7	76.44	72.5	0.31
Computational Value	-	-	-	<b>72.4</b>	<b>0.25</b>
Mean	35.2	107.6	72.4	<b>71.2</b>	<b>0.29</b>
Standard Deviation	3.8	3.1	3.6	<b>0.7</b>	<b>0.02</b>

Table 2: Statistics for 11 repeat runs at  $Re=8.1 \times 10^6/m$

## VI. Bispectral Analysis

### VI.A. Calculation of Bispectrum

The bicoherence spectrum was used to quantify the degree of nonlinear quadratic phase coupling among triads of wave frequencies. Quadratic phase coupling occurs when the sum of phase components of disturbances at frequencies  $f_1$  and  $f_2$  is equal to the phase of the disturbance at the sum or difference frequency ( $f_1 \pm f_2$ ).<sup>57</sup> That is,

$$f_1 \pm f_2 = f_3 \quad (11)$$

$$\angle f_1 \pm \angle f_2 = \angle f_3 \quad (12)$$

where  $\angle$  denotes the phase.

The bispectrum is defined as

$$B(f_1, f_2) = E[X(f_1)X(f_2)X^*(f_1 + f_2)] = \left| \frac{1}{N} \sum_{k=1}^N X_k(f_1)X_k(f_2)X_k^*(f_1 + f_2) \right| \quad (13)$$

where  $X$  denotes the Fourier Transform of a time series  $x(t)$ ,  $X^*$  is the complex conjugate of  $X$ , and  $N$  is the number of windows into which the time series is divided. Using this technique, it becomes clear that the bispectrum will average to 0 if the phase of  $X^*(f_1 + f_2)$  is random with respect to the phase of  $X(f_1)$  and  $X(f_2)$ . If it is quadratically coupled, however, the mean, and thus the bispectrum, will be nonzero.

The bicoherence is a normalized version of the bispectrum and quantifies the extent of quadratic phase coupling. The normalizing factor is maximized when  $f_1$ ,  $f_2$  and  $f_3$  are perfectly phase coupled. The normalizing factor used in this analysis was

Approved for public release; distribution unlimited.

11 of 17

American Institute of Aeronautics and Astronautics

$$\frac{1}{N} \sum_{k=1}^N |X_k(f_1)X_k(f_2)X_k^*(f_1 + f_2)| \quad (14)$$

By computing the absolute value before averaging, phase information is removed, effectively setting  $\angle f_1$ ,  $\angle f_2$ , and  $\angle f_3$  identically equal to 0 and enforcing perfect phase coupling for all frequency combinations. The bicoherence,

$$b^2(f_1, f_2) = \frac{|\frac{1}{N} \sum_{k=1}^N X_k(f_1)X_k(f_2)X_k^*(f_1 + f_2)|}{\frac{1}{N} \sum_{k=1}^N |X_k(f_1)X_k(f_2)X_k^*(f_1 + f_2)|} \quad (15)$$

then assumes a value from 0 to 1, with 0 indicating no nonlinear quadratic phase coupling, and 1 indicating complete quadratic phase coupling. References 40, 57–63 discuss the theoretical foundation and some applications of bispectral analysis.

## VI.B. Nonlinear Wave Coupling

The bispectral analysis was applied to the traveling crossflow data. Figure 10 shows contour plots of bicoherence for  $Re=8.9, 9.0, 9.7$ , and  $9.8 \times 10^6/m$  for sensor 5. For Reynolds numbers outside this range, the value of the bicoherence everywhere is small, indicating little phase coupling and low levels of nonlinear interactions. For reference, the PSD of the signal is plotted in red above the bicoherence. Units are not given and amplitudes are scaled in each case to fit within the plot area.

In all cases, the range of bicoherence displayed is from 0.20-0.40. Additionally, the bicoherence is symmetric about the  $f_2=f_1$  line, demarcated by a black diagonal line. Non-zero values of bicoherence along this line indicate wave self-interaction and the stimulation of harmonic modes. Since the bicoherence is symmetric about the  $f_2=f_1$  line, only values below this line are shown. Additionally, the Kulite sensors have a strong resonance at about  $f=280$  kHz. Frequency summations greater than 200 kHz are thus not shown.

For  $Re=8.9 \times 10^6/m$ , low levels of phase coupling are evident. Disturbances with frequencies ranging from 50-100 kHz show some phase locking with frequencies from 50-90 kHz in a broad sense, including some self-interaction. The peak bicoherence occurs for  $(f_1, f_2)=(75, 70)$  kHz, although the PSD does not have an apparent peak at  $f_1 + f_2=145$  kHz. The elevated levels of bicoherence for  $Re=8.9 \times 10^6/m$  comport well with the divergence of the  $\Psi$  and  $c_r$  curves for  $Re=8.9$  and  $9.0 \times 10^6/m$  in Figure 8, which were attributed to the onset of nonlinear processes.

As the Reynolds number increases to  $9.0 \times 10^6/m$ , the bicoherence shows interactions for the same frequencies as the  $Re=8.9 \times 10^6/m$  case, but with elevated bicoherence. The main interactions appear to be for  $f_1=62$  kHz and  $62 < f_2 < 138$  kHz. The corresponding PSD shows slightly elevated power for frequencies from 100-200 kHz, likely due to these broadband nonlinear interactions. This interaction is somewhat surprising since the main traveling crossflow peak is at about 45 kHz, which shows no phase locking with any frequencies.

The  $Re=9.7 \times 10^6/m$  condition exhibits the highest levels of bicoherence, though the maximum value is only about 0.42. Significant phase-coupling continues among  $f_1=62$  kHz and  $62 < f_2 < 138$  kHz disturbances is evident, contributing to both general spectral broadening as well as a peak in the PSD at 130 kHz. The PSD shows a marked disturbance at 62 kHz distinct from the main traveling crossflow peak. Additionally, a small peak in the PSD at about 7-10 kHz has developed and appears to be phase coupled with several other frequency bands, including the 62 kHz disturbance.

As  $Re$  is further increased to  $Re=9.8 \times 10^6/m$ , major distortions in the PSD continue, and the bicoherence amplitudes fall significantly. This likely indicates that the flow is transitional, and that phase-coupled disturbance relationships are destroyed by the random phases of the transitional boundary layer. The secondary peak at 62 kHz is more pronounced relative to the main traveling crossflow peak at 45 kHz for  $Re=9.8 \times 10^6/m$ . Additionally, significant spectral broadening is observed in the PSD. It appears that the wide bands of nonlinear interactions observed in the bicoherence for  $Re=9.0$  and  $9.7 \times 10^6/m$  transfer energy into the higher frequencies of the spectrum, while the low-frequency interactions, observed primarily for  $Re=9.7 \times 10^6/m$ , contribute to the low-frequency spectral broadening.

For higher Reynolds numbers (not shown), the bicoherence levels fall further, indicating a turbulent boundary layer. The significance of the maximum value that the bicoherence achieved, 0.42, is unclear. Kimmel and Kendall<sup>62</sup> cite a bicoherence value of 0.4 as being “high.” They report this as a high value

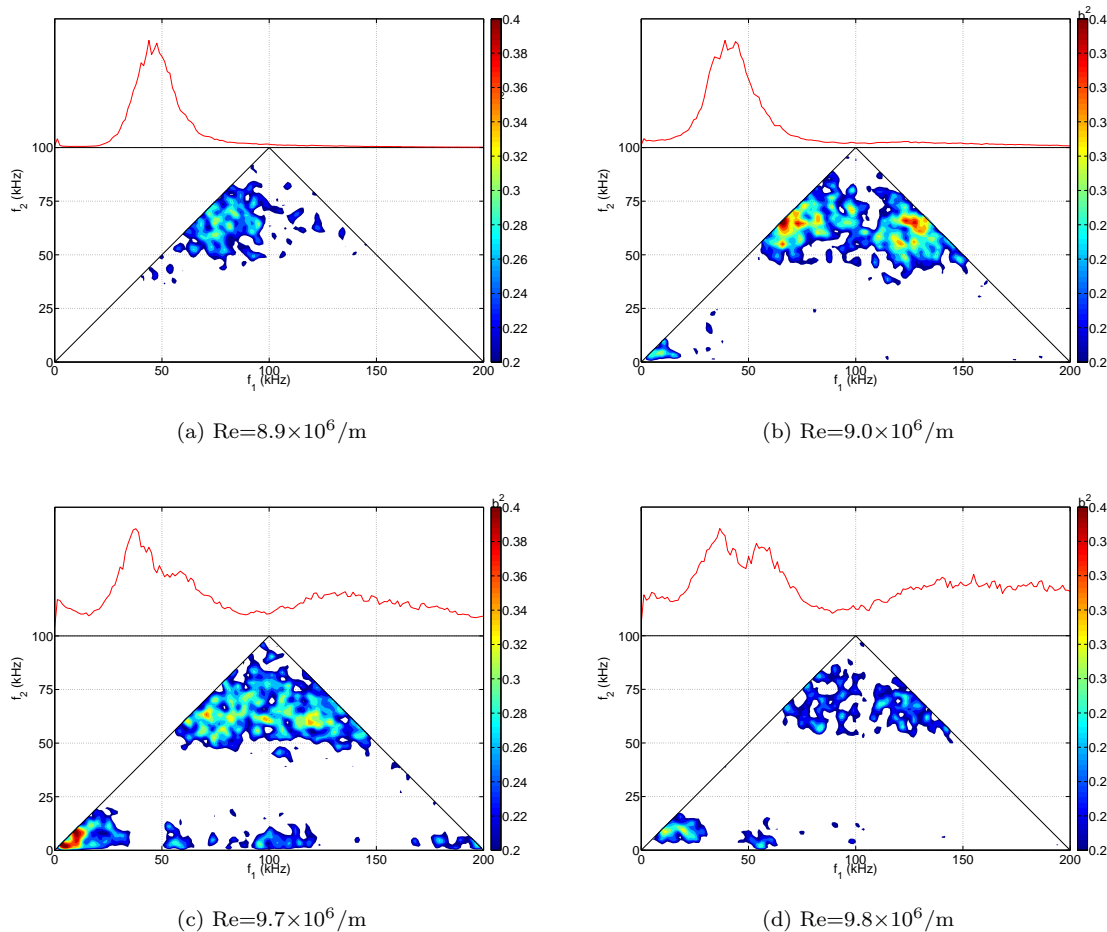


Figure 10: Bicoherence and PSD for  $\text{Re}=8.9\text{-}9.8 \times 10^6/\text{m}$  for sensor 5



because their signal-to-noise ratio was near unity. The signal-to-noise is considerably better in the present experiments. Chokani<sup>57</sup> observed bicoherence levels as high as 0.9 for second mode waves.

The lack of any significant nonlinear interactions involving the primary traveling crossflow wave at 45 kHz suggests that the traveling mode may not be the primary instability mechanism responsible for transition under quiet conditions. It may be that, as expected in quiet freestream environments, the stationary mode is ultimately responsible for transition. The cause of the secondary peak that appears in the PSDs for  $Re=9.7$  and  $9.8 \times 10^6/m$  is unclear, though it may be a secondary instability of the stationary modes.

## VII. Noisy Flow

The freestream noise level was increased to “conventional” levels and a Reynolds number sweep from  $Re=0.4$ - $5.5 \times 10^6/m$  was performed. Traveling crossflow waves were expected since they were observed at the lower “quiet” freestream noise level.

Figure 11 shows PSDs for all noisy Reynolds numbers. Two quiet PSDs are also included for reference. The quiet  $Re=8.3 \times 10^6/m$  condition represents laminar flow with large traveling crossflow waves. The quiet  $Re=12.4 \times 10^6/m$  case demonstrates a turbulent model boundary layer with quiet freestream flow. A PSD of the sensor output with quiescent air at vacuum, representative of the electronic noise floor, is also shown.

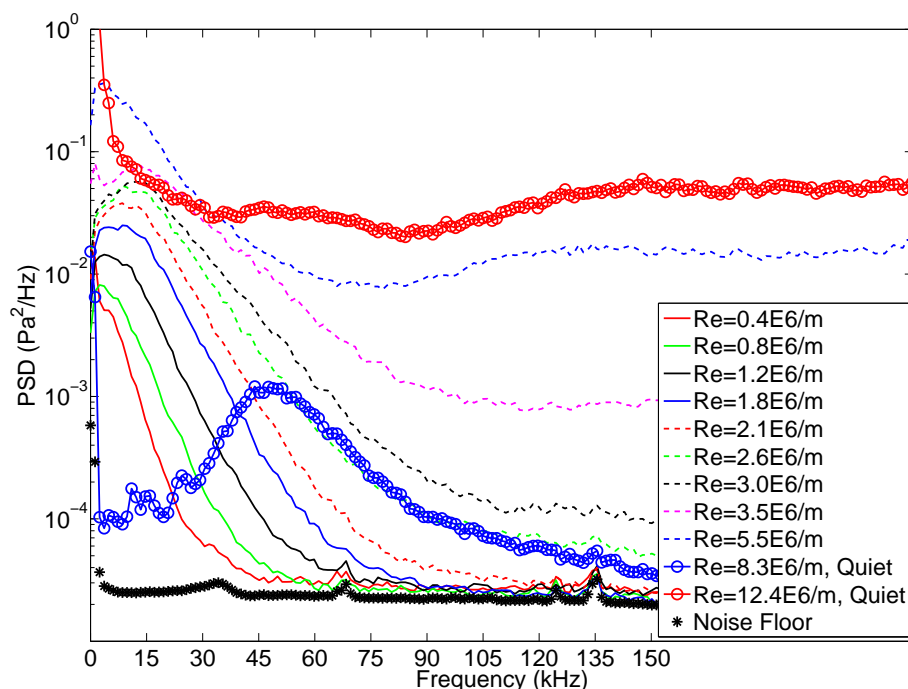


Figure 11: PSD for noisy flow,  $Re=0.4$ - $5.5 \times 10^6/m$ , sensor 3

The  $Re=0.4 \times 10^6/m$  condition represents the lowest Reynolds number at which the BAM6QT can operate. The spectrum for this condition is likely laminar since the power drops quickly from its initial value at 0 kHz to the electronic noise floor for frequencies greater than about 40 kHz. The highest Reynolds number condition,  $Re=5.5 \times 10^6/m$  appears to be nearly turbulent since it approaches the quiet,  $Re=12.4 \times 10^6/m$  turbulent spectrum.

Although spectra with elevated freestream noise are shown spanning from fully laminar to fully turbulent conditions, there is no evidence of the prominent 40-50 kHz traveling waves seen with quiet flow. This lack of traveling crossflow waves is surprising.

The initial amplitudes of traveling crossflow waves are determined by vortical disturbances in the incoming flow.<sup>36</sup> With elevated freestream noise, the freestream Reynolds number is considerably below that for which traveling crossflow waves were measured in quiet flow. It is possible that the traveling crossflow growth rates at these reduced freestream Reynolds numbers are so low that traveling crossflow waves do not

amplify sufficiently to be measured prior to boundary layer transition. Additionally, the freestream vortical disturbances at these reduced Reynolds numbers may be of lower amplitude than for the higher Reynolds number quiet cases, giving the traveling crossflow a lower initial amplitude. The absence of observable traveling crossflow waves in noisy flow while they are prominent in quiet flow is different from what has been observed for the second mode instability on a circular cone. In this case, second mode waves are seen in both noisy and quiet flow at the same Reynolds number in Purdue's tunnel. However, the amplitude of the second-mode waves is about 2 orders of magnitude lower for quiet flow than noisy flow.<sup>64</sup>

This explanation accounts for the lack of measured traveling crossflow waves, but does not account for the transition mechanism. It seems evident that at this reduced Reynolds number and increased freestream noise, the dominant transition mechanism is not the traveling crossflow instability. In a previous study,<sup>50</sup> stationary crossflow vortices were seen in oil flow for noisy flow at higher Reynolds numbers than those in the present experiments, but never in the TSP images. This behavior implies that the stationary crossflow modes in noisy flow do not reach the amplitudes that they do in quiet flow. Under noisy flow, transition is not caused by traveling crossflow instabilities. Under noisy flow, transition appears to be the result of broadband growth of lower-frequency disturbances. The precise nature of the lower-frequency disturbances is uncertain and remains under investigation.

## VIII. Summary and Conclusions

A traveling crossflow instability was clearly measured for the HIFiRE-5 in quiet flow using surface-mounted pressure sensors. The frequency, phase speed, and wave angle were measured and were all in good agreement with computations. The peak frequency at  $Re=8.3 \times 10^6/m$  shows good repeatability. The amplitudes of the PSDs was shown to increase over the course of a day. This increase is thought to be due to the increasing model surface temperature with each subsequent run. It is possible that the increased surface temperature destabilizes the traveling crossflow instability.

The traveling crossflow waves were observed to undergo a period of what appears to be primarily linear growth over a Reynolds number range from about  $6.8-8.5 \times 10^6/m$  for sensor 5. Bispectral analysis showed some nonlinear interactions for  $Re=8.9-9.8 \times 10^6/m$ , but not at frequencies corresponding to the peak traveling crossflow frequency. Higher Reynolds numbers then led to transition onset and turbulent flow. For the freestream Reynolds numbers showing no nonlinear processes, wave angle and phase speed matched the computations well over a range of frequencies. When nonlinear effects became significant, both wave angle and phase speed diverged considerably from the values observed for lower Reynolds numbers. The lack of nonlinear interactions involving the peak traveling crossflow frequency suggests that, although traveling crossflow disturbances are prominent in the surface pressure spectrum, they may not play a dominant role in the transition process.

No traveling crossflow waves were observed in noisy flow. This is thought to be due to a smaller area of the model being unstable to the traveling crossflow instability at the lower Reynolds numbers for which the model boundary layer was laminar with noisy flow. The dominant instability mechanism for low Reynolds number noisy flow is unknown, but analysis is ongoing.

## Acknowledgments

The authors are grateful to Prof. Steven Schneider of Purdue University for donating time in the BAM6QT for these experiments. Prof. Schneider's research group was very helpful in supporting these tests. Thanks are also due to Dr. Thomas Juliano for his assistance, providing valuable insight into the experiments and the model based on his previous experience, as well as for several fruitful discussions of the data. Dr. Meelan Choudhari of NASA LaRC performed the computations. This work was supported by Dr. John Schmisser of AFOSR/RTE.

## References

- <sup>1</sup>Dolvin, D., "Hypersonic International Flight Research and Experimentation (HIFiRE) Fundamental Science and Technology Development Strategy," AIAA paper 2008-2581, April 2008.
- <sup>2</sup>Dolvin, D., "Hypersonic International Flight Research and Experimentation Technology Development and Flight Certification Strategy," AIAA paper 2009-7228, Oct. 2009.
- <sup>3</sup>Kimmel, R. L., Adamczak, D., Gaitonde, D., Rougeux, A., and Hayes, J. R., "HIFiRE-1 Boundary Layer Transition

Approved for public release; distribution unlimited.

15 of 17

American Institute of Aeronautics and Astronautics

Experiment Design," AIAA paper 2007-0534, Jan. 2009.

<sup>4</sup>Wadhams, T. P., MacLean, M. G., Holden, M. S., and Mudy, E., "Pre-Flight Ground Testing of the Full-Scale FRESH FX-1 at Fully Duplicated Flight Conditions," AIAA paper 2007-4488, June 2007.

<sup>5</sup>Johnson, H. B., Alba, C. R., Candler, G. V., MacLean, M., Wadhams, T., and Holden, M., "Boundary Layer Stability Analysis of the Hypersonic International Flight Research Transition Experiments," *Journal of Spacecraft and Rockets*, Vol. 45, No. 2, March-April 2008, pp. 194-204.

<sup>6</sup>Holden, M. S., Wadhams, T. P., and MacLean, M., "Experimental Studies in the LENS Supersonic and Hypersonic Tunnels for Hypervelocity Vehicle Performance and Code Validation," AIAA paper 2008-2505, April 2008.

<sup>7</sup>Kimmel, R. L., "Aerothermal Design for the HIFiRE-1 Flight Vehicle," AIAA paper 2008-4034, June 2008.

<sup>8</sup>Casper, K. M., Wheaton, B. M., Johnson, H. B., and Schneider, S. P., "Effect of Freestream Noise on Roughness-Induced Transition at Mach 6," AIAA paper 2008-4291, June 2008.

<sup>9</sup>Kimmel, R. L., "Roughness Considerations for the HIFiRE-1 Vehicle," AIAA paper 2008-4293, June 2008.

<sup>10</sup>Alba, C. R., Johnson, H. B., Bartkiewicz, M. D., Candler, G. V., and Berger, K. T., "Boundary-Layer Stability Calculations for the HIFiRE-1 Transition Experiment," *Journal of Spacecraft and Rockets*, Vol. 45, No. 6, November-December 2008, pp. 1125-1133.

<sup>11</sup>Wadhams, T. P., Mundy, E., MacLean, M. G., and Holden, M. S., "Ground Test Studies of the HIFiRE-1 Transition Experiment Part 1: Experimental Results," *Journal of Spacecraft and Rockets*, Vol. 45, No. 6, November-December 2008, pp. 1134-1148.

<sup>12</sup>MacLean, M. G., Wadhams, T. P., Holden, M. S., and Johnson, H. B., "Ground Test Studies of the HIFiRE-1 Transition Experiment Part 2: Computational Analysis," *Journal of Spacecraft and Rockets*, Vol. 45, No. 6, November-December 2008, pp. 1149-1164.

<sup>13</sup>Berger, K. T., Greene, F. A., Kimmel, R. L., Alba, C., and Johnson, H., "Erratum on Aerothermodynamic Testing and Boundary-Layer Trip Sizing of the HIFiRE Flight 1 Vehicle," *Journal of Spacecraft and Rockets*, Vol. 46, No. 2, March-April 2009, pp. 473-480.

<sup>14</sup>Adamczak, D., Alesi, H., and Frost, M., "HIFiRE-1: Payload Design, Manufacture, Ground Test, and Lessons Learned," AIAA paper 2009-7294, Oct. 2009.

<sup>15</sup>Malik, M. R., Li, F., and Choudhari, M., "Analysis of Crossflow Transition Flight Experiment Aboard the Pegasus Launch Vehicle," AIAA paper 2007-4487, June 2007.

<sup>16</sup>Laderman, A., "Review of Wind-Tunnel Freestream Pressure Fluctuations," *AIAA Journal*, Vol. 15, No. 4, April 1977, pp. 605-608.

<sup>17</sup>Schneider, S. P., "Effects of high-speed tunnel noise on laminar-turbulent transition," *Journal of Spacecraft and Rockets*, Vol. 38, No. 3, May-June 2001, pp. 323-333.

<sup>18</sup>Reed, H. L., Kimmel, R., Schneider, S., and Arnal, D., "Drag prediction and transition in hypersonic flow," Paper 97-1818, AIAA, June 1997.

<sup>19</sup>Pate, S. and Schuele, C., "Radiated aerodynamic noise effects on boundary-layer transition in supersonic and hypersonic wind tunnels," *AIAA Journal*, Vol. 7, No. 3, 1969, pp. 450-457.

<sup>20</sup>Chen, F.-J., Malik, M., and Beckwith, I., "Boundary-layer transition on a cone and flat plate at Mach 3.5," *AIAA Journal*, Vol. 27, No. 6, 1989, pp. 687-693.

<sup>21</sup>Ito, T., Randall, L. A., and Schneider, S. P., "Effect of Noise on Roughness-Induced Boundary-Layer Transition for Scramjet Inlet," *Journal of Spacecraft and Rockets*, Vol. 38, No. 5, 2001, pp. 692-698.

<sup>22</sup>Borg, M. P. and Schneider, S. P., "Effect of Freestream Noise on Roughness-Induced Transition for the X-51A Forebody," *Journal of Spacecraft and Rockets*, Vol. 45, No. 6, November-December 2008, pp. 1106-1116.

<sup>23</sup>Laufer, J., "Aerodynamic Noise in supersonic wind tunnels," *Journal of the Aerospace Sciences*, Vol. 28, No. 9, 1961, pp. 685-692.

<sup>24</sup>Palmerio, A. F., da Silva, J. P. C. P., Turner, P., and Jung, W., "The development of the VSB-30 sounding rocket vehicle," *ESA SP-530: 16th ESA Symposium on European Rocket and Balloon Programmes and Related Research*, edited by B. Warmbein, ESA Publications Division, Noordwijk, 2003, pp. 137-140.

<sup>25</sup>"NASA Sounding Rocket Program Handbook," 810-hb-srp, Sounding Rockets Program Office, Suborbital & Special Orbital Projects Directorate, Goddard Space Flight Center, Wallops Island Flight Facility, June 2005.

<sup>26</sup>Kimmel, R. L. and Poggie, J., "Transition on an Elliptic Cone at Mach 8," American Society of Mechanical Engineers ASME FEDSM97-3111, June 1997.

<sup>27</sup>Kimmel, R. L. and Poggie, J. J., "Three-Dimensional Hypersonic Boundary Layer Stability and Transition," WL-TR-97-3111, Air Force Research Laboratory Technical Report, Wright-Patterson Air Force Base, Ohio, Dec. 1997.

<sup>28</sup>Kimmel, R. L., Poggie, J. J., and Schwoerke, S. N., "Laminar-Turbulent Transition in a Mach 8 Elliptic Cone Flow," *AIAA Journal*, Vol. 37, No. 9, September 1999, pp. 1080-1087.

<sup>29</sup>Schmisser, J., *Receptivity of the Boundary Layer on a Mach-4 Elliptic Cone to Laser-Generated Localized Freestream Perturbations*, Ph.D. thesis, Purdue University, Dec. 1997.

<sup>30</sup>Holden, M., "Experimental Studies of Laminar, Transitional, and Turbulent Hypersonic Flows Over Elliptic Cones at Angle of Attack," Technical report AFRL-SR-BL-TR-98-0142, Air Force Office of Scientific Research, Bolling Air Force Base, Washington D.C., Dec. 1998.

<sup>31</sup>Schmisser, J., Schneider, S. P., and Collicott, S. H., "Receptivity of the Mach 4 Boundary Layer on an Elliptic Cone to Laser-Generated Localized Freestream Perturbations," AIAA paper 1998-0532, Jan. 1998.

<sup>32</sup>Schmisser, J., Schneider, S. P., and Collicott, S. H., "Response of the Mach 4 boundary layer on an elliptic cone to laser-generated freestream perturbations," AIAA paper 1999-0410, Jan. 1999.

<sup>33</sup>Lytle, I. J. and Reed, H., "Use of Transition Correlations for Three-Dimensional Boundary Layers Within Hypersonic Flows," AIAA paper 1995-2293, June 1995.

- <sup>34</sup>Malik, M., Li, F., and Chang, C.-L., "Crossflow disturbances in three-dimensional boundary layers: nonlinear development, wave interaction and secondary instability," *Journal of Fluid Mechanics*, Vol. 268, 1994, pp. 1–36.
- <sup>35</sup>Saric, W. S. and Reed, H. L., "Crossflow Instabilities- Theory & Technology," AIAA paper 2003-0771, Jan. 2003.
- <sup>36</sup>Bippes, H., "Basic experiments on transition in three-dimensional boundary layers dominated by crossflow instability," *Progress in Aerospace Sciences*, Vol. 35, 1999, pp. 363–412.
- <sup>37</sup>Saric, W. S. and Reed, H. L., "Supersonic Laminar flow control on swept wings using distributed roughness," AIAA paper 2002-0147, Jan. 2002.
- <sup>38</sup>Bippes, H. and Lerche, T., "Transition Prediction in Three-Dimensional Boundary-Layer Flows Unstable to Crossflow Instability," AIAA paper 97-1906, 1997.
- <sup>39</sup>Carpenter, M. H., Choudhari, M., Li, F., Streett, C. L., and Chang, C.-L., "Excitation of Crossflow Instabilities in a Swept Wing Boundary Layer," Paper 2010-0378, AIAA, January 2010.
- <sup>40</sup>Eppink, J. and Wlezién, R., "Observations of traveling crossflow resonant triad interactions on a swept wing," Paper 2012-2820, AIAA, June 2012.
- <sup>41</sup>White, E. B. and Saric, W. S., "Secondary instability of crossflow vortices," *Journal of Fluid Mechanics*, Vol. 525, 2005, pp. 275–308.
- <sup>42</sup>King, R., "Three-dimensional boundary-layer transition on a cone at Mach 3.5," *Experiments in Fluids*, Vol. 13, No. 4, 1992, pp. 305–314.
- <sup>43</sup>Poggie, J., Kimmel, R. L., and Schwoerke, S. N., "Traveling Instability Waves in a Mach 8 Flow over an Elliptic Cone," *AIAA Journal*, Vol. 38, No. 2, 2000, pp. 251–258.
- <sup>44</sup>Choudhari, M., Chang, C.-L., Jentink, T., Li, F., Berger, K., Candler, G., and Kimmel, R., "Transition Analysis for the HIFiRE-5 Vehicle," AIAA paper 2009-4056, June 2009.
- <sup>45</sup>Swanson, E. O. and Schneider, S. P., "Boundary-layer transition on cones at angle of attack in a Mach-6 quiet tunnel," Paper 2010-1062, AIAA, January 2010.
- <sup>46</sup>Borg, M. P., Kimmel, R. L., and Stanfield, S., "Crossflow Instability for HIFiRE-5 in a Quiet Hypersonic Wind Tunnel," Paper 2012-2821, AIAA, June 2012.
- <sup>47</sup>Juliano, T. J. and Schneider, S. P., "Instability and Transition on the HIFiRE-5 in a Mach-6 Quiet Tunnel," AIAA paper 2010-5004, June 2010.
- <sup>48</sup>Schneider, S. P., "Design of a Mach-6 quiet-flow wind-tunnel nozzle using the e\*\*N method for transition estimation," AIAA paper 98-0547, Jan. 1998.
- <sup>49</sup>Beresh, S. J., Henfling, J., Spillers, R., and Pruett, B., "Measurements of Fluctuating Wall Pressures Beneath a Supersonic Turbulent Boundary Layer," Paper 2010-0305, AIAA, January 2010.
- <sup>50</sup>Borg, M. P., Kimmel, R. L., and Stanfield, S., "HIFiRE-5 Attachment-line transition in a Quiet Hypersonic Wind Tunnel," Paper 2011-3247, AIAA, June 2011.
- <sup>51</sup>Schneider, S. P., Collicott, S. H., Schmisser, J. D., Ladoon, D., Randall, L. A., Munro, S. E., and Salyer, T. R., "Laminar-turbulent transition research in the Purdue Mach-4 Quiet-Flow Ludwig Tube," AIAA paper 96-2191, June 1996.
- <sup>52</sup>Li, F., Choudhari, M., Chang, C.-L., White, J., Kimmel, R., Adamczak, D., Borg, M., Stanfield, S., and Smith, M., "Stability Analysis for HIFiRE Experiments," AIAA paper 2012-2961, June 2012.
- <sup>53</sup>Bendat, J. and Piersol, A., *Engineering Applications of Correlation and Spectral Analysis*, Wiley-Interscience, 1980.
- <sup>54</sup>Choudhari, M., Private communication, Aug. 2012.
- <sup>55</sup>Juliano, T. J., *Instability and transition on the HIFiRE-5 in a Mach-6 quiet tunnel*, Ph.D dissertation, Purdue University (West Lafayette), August 2010, School of Aeronautics and Astronautics.
- <sup>56</sup>Eppink, J. and Wlezién, R., "Data analysis for the NASA/Boeing hybrid laminar flow control crossflow experiment," Paper 2011-3879, AIAA, June 2011.
- <sup>57</sup>Chokani, N., "Nonlinear spectral dynamics of hypersonic laminar boundary layer flow," *Physics of Fluids*, Vol. 11, No. 12, Dec. 1999.
- <sup>58</sup>Chokani, N., "Nonlinear stability of quiet tunnel hypersonic laminar boundary layer flow," Paper 99-0407, AIAA, January 1999.
- <sup>59</sup>Norris, J. and Chokani, N., "Three-wave coupling in a transitional hypersonic boundary layer," AIAA paper 2001-2780, June 2001.
- <sup>60</sup>Kim, Y. and Powers, E. J., "Digital bispectral analysis of self-excited fluctuation spectra," *Physics of Fluids*, Vol. 21, No. 8, 1978.
- <sup>61</sup>Kim, Y. C. and Powers, E. J., "Digital bispectral analysis and its applications to nonlinear wave interactions," *IEEE Transactions on Plasma Science*, Vol. PS-7, No. 2, 1979.
- <sup>62</sup>Kimmel, R. L. and Kendall, J. M., "Nonlinear disturbances in a hypersonic laminar boundary layer," AIAA paper 91-0320, June 1991.
- <sup>63</sup>Shiplyuk, A. N., Bountin, D. A., Maslov, A. A., and Chokani, N., "Nonlinear interactions of second mode instability with natural and artificial disturbances," AIAA paper 2003-0787, Jan. 2003.
- <sup>64</sup>Estorfe, M., Radespiel, R., Schneider, S. P., Johnson, H. B., and Hein, S., "Surface-pressure measurements of second-mode instability in quiet hypersonic flow," Paper 2008-1153, AIAA, January 2008.